

# RESPLE: Recursive Spline Estimation for LiDAR-Based Odometry

Ziyu Cao, William Talbot, and Kailai Li

**Abstract**— We present a novel recursive Bayesian estimation framework for continuous-time six-DoF dynamic motion estimation using B-splines. The state vector consists of a recurrent set of position control points and orientation control point increments, enabling a straightforward modification of the iterated extended Kalman filter without involving the error-state formulation. The resulting recursive spline estimator (RESPLE) provides a versatile, pragmatic and lightweight solution for motion estimation and is further exploited for direct LiDAR-based odometry, supporting integration of one or multiple LiDARs and an IMU. We conduct extensive real-world benchmarking based on public datasets and own experiments, covering aerial, wheeled, legged, and wearable platforms operating in indoor, urban, wild environments with diverse LiDARs. RESPLE-based solutions achieve superior estimation accuracy and robustness over corresponding state-of-the-art systems, while attaining real-time performance. Notably, our LiDAR-only variant outperforms existing LiDAR-inertial systems in scenarios without significant LiDAR degeneracy, and showing further improvements when additional LiDAR and inertial sensors are incorporated for more challenging conditions. We release the source code and own experimental datasets at <https://github.com/ASIG-X/RESPLE>.

**Index Terms**— State estimation, sensor fusion, LiDAR.

## I. INTRODUCTION

Reliable estimation of dynamic egomotions using on-board sensors is critical for mobile robots to achieve high-performance autonomy in ubiquitous application scenarios, such as autonomous driving, service robotics, search and rescue, perceptive locomotion, and navigation [1]–[3]. Multi-sensor solutions involving light detection and ranging (LiDAR) sensors, have gained significant popularity due to their inherent advantages over vision-based perception. These include resilience to varying lighting conditions, spatiotemporally dense observations, high accuracy, and long detection range. Additionally, recent advances in lightweight, versatile designs, and improved cost-effectiveness have further fueled the adoption of LiDAR in robotic systems [4]–[6].

Traditionally, dynamic motion estimation has been addressed in the discrete-time domain, where states are estimated often at a fixed rate via filtering or nonlinear optimization (smoothing). The former, such as the error-state Kalman filter, recursively predicts and updates state estimates according to predefined process and measurement models [7], [8]. The latter, often applied in a sliding-window fashion, optimizes states via maximum likelihood estimation

Ziyu Cao is with Department of Electrical Engineering, Linköping University, Sweden. William Talbot is with Robotic Systems Lab (RSL), ETH Zurich, Switzerland. Kailai Li is with Bernoulli Institute for Mathematics, Computer Science and Artificial Intelligence, University of Groningen, The Netherlands. E-mails: [ziyu.cao@liu.se](mailto:ziyu.cao@liu.se), [wtalbot@ethz.ch](mailto:wtalbot@ethz.ch), [kailai.li@rug.nl](mailto:kailai.li@rug.nl).

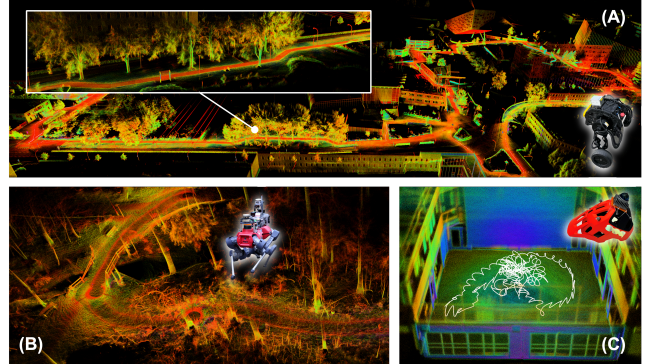


**Fig. 1:** RESPLE-LO tested on (A) a wheeled bipedal robot in a campus environment, (B) a quadruped robot in the wild, and (C) a helmet platform indoor in highly dynamic motions.

(MLE) or maximum a posteriori (MAP) estimation [4], [6], [9], [10]. Both methodologies have well established solutions for LiDAR-based odometry combining efficient map representation, such as the ikd-Tree [11] and iVox [12], with per-point residuals using point-to-point or point-to-plane metrics, achieving real-time performance [5], [13]. The inertial measurement unit (IMU) is commonly integrated for explicit motion compensation of LiDAR scans or better handling dynamic motions in general. However, in the presence of spatiotemporally dense and asynchronous observations from multiple sensors, discrete-time methods face limitations in high-fidelity processing, accommodating varying sensor rates, and maintaining estimation accuracy without incurring excessive theoretical or computational complexity [14].

The continuous-time paradigm provides effective alternatives for estimating dynamic motion and is of increasing interest in LiDAR-based odometry for mobile robotics. Common choices of continuous-time motion models include piecewise-linear functions, Gaussian processes (GPs) and B-splines, whereby interpolated residuals can be computed for estimation [14], [15]. The piecewise-linear function representation is well motivated by the constant-velocity assumption applied in LiDAR scan de-skewing [6], [16] and has been embraced in recent continuous-time LiDAR odometry and SLAM systems [17]. However, applying this piecewise constant-velocity assumption cannot fully capture dynamic motion in modern robotic systems, motivating an exploration of more expressive representations. Interpolation with ‘exactly sparse’ GPs has emerged as an effective continuous-time motion estimation approach [18], [19]. The interpolation scheme itself emerges from a chosen motion model, with constant-velocity and constant-acceleration being common choices, and has been applied in various LiDAR-based

estimation pipelines [20]–[22]. B-splines (usually uniform and cubic) remain a particularly popular representation for solving various multi-sensor trajectory estimation problems, especially for high-rate sensors like LiDARs, ultra-wideband and IMUs [23], [24]. Several LiDAR-inertial odometry (LIO) systems have been developed based upon this representation and demonstrate promising gains in estimation accuracy and robustness [25]–[28]. However, B-spline-based continuous-time LiDAR or multi-LiDAR odometry remains underexplored in practice, especially with open-source contributions.

Most continuous-time estimation approaches adopt the strategy of tightly-coupled MLE or MAP optimization incorporating multi-sensor interpolated residuals. This importantly avoids motion compensation of LiDAR scans as a preprocessing step since it is implicitly accounted for and enables incorporation of high-rate, asynchronous sensor data at their exact timestamps. However, the optimization-based designs rely on high-performance and often customized solvers, which pose significant challenges in computational efficiency and versatility, especially in multi-sensor settings for mobile applications [24], [25].

In contrast, recursive Bayesian estimation offers a conceptually lightweight, computationally efficient, and pragmatic alternative, which has been well adopted in discrete-time LIO [5], [13], yet has seen very limited exploration in the continuous-time paradigm [22], [29]. To this end, a B-spline-based recursive estimation scheme was conceptualized in [30], albeit limited to tracking only Euclidean states. Meanwhile, CTE-MLO [22] enabled multi-LiDAR odometry via extended Kalman filter (EKF) based on GPs, where a localizability-based LiDAR point sampling strategy is additionally devised to achieve real-time performance and environmental robustness. To the authors’ best knowledge, B-spline-based recursive Bayesian estimation has not yet been introduced for estimating 6-DoF dynamic motions, including its application to LiDAR-based odometry.

### Contribution

We introduce RESPLE (**R**ecursive **S**pline Estimator), the first B-spline-based recursive estimation framework for 6-DoF dynamic motion estimation. Cubic B-splines representing 6-DoF continuous-time motion are embedded into state-space modeling and estimated through a modified iterated EKF without involving error-state formulations. Using RESPLE as the estimation backbone, we develop a versatile suite of direct LiDAR-based odometry systems, enabling LiDAR, LiDAR-inertial, multi-LiDAR, and multi-LiDAR-inertial odometry, all within a unified system design. We conduct extensive real-world evaluations using public datasets and experiments across diverse application scenarios. RESPLE-based solutions consistently outperform state-of-the-art counterparts in terms of estimation accuracy and robustness with real-time efficiency. Notably, our LiDAR-only odometry system surpasses existing LiDAR-inertial solutions in scenarios without significant geometric degeneracy, with enhanced robustness enabled by including additional sensors under more challenging conditions. RESPLE shows a

strong potential as a universal multi-sensor motion estimation framework, and we release our complete implementation and experimental datasets to the public.

## II. PRELIMINARIES

### A. Notation Conventions

Throughout the following content, scalar values are written as lowercase letters, such as  $a$ . We use underlined lowercase letters, such as  $\underline{a}$ , to denote vectors and bold capital letters, such as  $\mathbf{A}$ , for matrices. Continuous functions are denoted by italic letters, such as  $\mathcal{J}(t)$ . Operators  $\bullet$  and  $\otimes$  are used to denote the Hamilton and Kronecker product, respectively.

### B. Continuous-Time Parameterization of 6-DoF Motions

We exploit cubic B-splines (fourth-order) to represent 6-DoF motions in the continuous-time domain [24] as follows

$$\mathbf{x}(t) = [\mathcal{J}(t)^\top, \mathcal{r}(t)^\top]^\top \in \mathbb{R}^3 \times \mathbb{S}^3 \subset \mathbb{R}^7. \quad (1)$$

$\mathcal{J}(t)$  and  $\mathcal{r}(t)$  are the position and quaternion-valued orientation spline components, respectively, determined by the control points,  $\{\underline{s}_i\}_{i=1}^n$  and  $\{\mathbf{r}_i\}_{i=1}^n$  over knots  $\{t_i\}_{i=1}^n$  with a uniform temporal interval  $\tau$ . The separation of poses into their position and orientation components is supported in literature [24], [31], [32], with the decoupling more computationally efficient and more appropriate for handheld and mobile robot motions. Given an arbitrary time instant  $t \in [t_{n-1}, t_n)$ , the position can be obtained according to

$$\mathcal{J}(t) = [\underline{s}_{n-3}, \underline{s}_{n-2}, \underline{s}_{n-1}, \underline{s}_n] \mathbf{\Omega} \underline{u}, \quad \text{with} \quad (2)$$

$$\mathbf{\Omega} = \frac{1}{6} \begin{bmatrix} 1 & -3 & 3 & -1 \\ 4 & 0 & -6 & 3 \\ 1 & 3 & 3 & -3 \\ 0 & 0 & 0 & 1 \end{bmatrix} \quad \text{and} \quad \underline{u} = [1, u, u^2, u^3]^\top \quad (3)$$

denoting the basis matrix and powers of normalized time

$$u = (t - t_{n-1})/\tau, \quad (4)$$

respectively. Similarly, the quaternion-valued B-spline in (1) at  $t \in [t_{n-1}, t_n)$  takes the following cumulative expression

$$\mathcal{r}(t) = \mathbf{r}_{n-4} \bullet \prod_{i=n-3}^n \text{Exp}_{\mathbb{1}}(\lambda_i \underline{\delta}_i). \quad (5)$$

$\underline{\delta}_i$  is the increment of adjacent control points measured in the tangent space with

$$\underline{\delta}_i = \text{Log}_{\mathbb{1}}(\mathbf{r}_{i-1}^{-1} \bullet \mathbf{r}_i), \quad \text{for } i = n-3, \dots, n. \quad (6)$$

$\text{Log}_{\mathbb{1}}(\cdot)$  and  $\text{Exp}_{\mathbb{1}}(\cdot)$  are the logarithm and exponential maps at identity quaternion  $\mathbb{1} = [1, 0, 0, 0]^\top$  [7]. In accordance with the cumulative B-spline in (5), the cumulative basis functions  $\{\lambda_i\}_{i=n-3}^n$  are given by

$$[\lambda_{n-3}, \lambda_{n-2}, \lambda_{n-1}, \lambda_n]^\top = \mathbf{\Phi} \underline{u}, \quad (7)$$

where the cumulative basis matrix [23] follows

$$\mathbf{\Phi} = \frac{1}{6} \begin{bmatrix} 6 & 0 & 0 & 0 \\ 5 & 3 & -3 & 1 \\ 1 & 3 & 3 & -2 \\ 0 & 0 & 0 & 1 \end{bmatrix}.$$

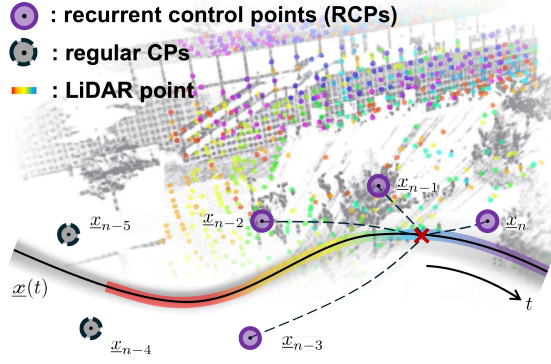


**Fig. 2:** Conceptual illustration of RESPLE-LO. LiDAR points with exact timestamps (colored) recursively update B-spline trajectory (black curve) with uncertainties (gray band).

### C. Kinematic Interpolations

We now present kinematic interpolations on the six-DoF B-spline in IMU-involved multi-sensor settings, including temporal derivatives of the position and orientation components up to the second and the first order, respectively.

1) *Positions:* The position B-spline in (2) has a linear expression w.r.t. the normalized time vector  $\underline{u}$ . According to [30], it is straightforward to derive the following generic expression for position kinematics via vectorization of (2)

$$\begin{aligned} \dot{\mathcal{J}}(t) &= \dot{\mathbf{A}} [\underline{s}_{n-3}^\top, \underline{s}_{n-2}^\top, \underline{s}_{n-1}^\top, \underline{s}_n^\top]^\top, \quad \text{with} \\ \dot{\mathbf{A}} &= (\mathbf{\Omega} \dot{\underline{u}})^\top \otimes \mathbf{I}_3 \in \mathbb{R}^{3 \times 12}. \end{aligned} \quad (8)$$

‘ $\circ$ ’ serves as an umbrella symbol for the zeroth- to second-order temporal derivatives of the function underneath, such as position  $\mathcal{J}(t)$ , velocity  $\dot{\mathcal{J}}(t)$ , and acceleration  $\ddot{\mathcal{J}}(t)$ . Derivatives of the normalized time vector  $\underline{u}$  can be derived given (4).

2) *Orientations:* In accordance with gyroscope observations, we provide the first-order temporal derivative of the orientation B-spline (5), namely, the angular velocity function  $\underline{\omega}(t)$  w.r.t. the body frame. This follows the recursive computation procedure presented in [24]

$$\begin{aligned} \underline{\omega}_1(t) &= 2\dot{\lambda}_{n-2} \delta_{n-2}, \\ \underline{\omega}_2(t) &= \underline{e}_{n-1}^{-1} \bullet \underline{\omega}_1(t) \bullet \underline{e}_{n-1} + 2\dot{\lambda}_{n-1} \delta_{n-1}, \\ \underline{\omega}(t) &= \underline{e}_n^{-1} \bullet \underline{\omega}_2(t) \bullet \underline{e}_n + 2\dot{\lambda}_n \delta_n, \end{aligned} \quad (9)$$

with  $\underline{e}_i = \text{Exp}_{\mathbf{1}}(\lambda_i \delta_i)$ , for  $i = n-1$  and  $n$ . The derivatives of the cumulative basis functions in (7) are given by  $[\dot{\lambda}_{n-3}, \dot{\lambda}_{n-2}, \dot{\lambda}_{n-1}, \dot{\lambda}_n]^\top = \mathbf{\Phi} \dot{\underline{u}}$ .

## III. RECURSIVE MOTION ESTIMATION ON B-SPLINES

### A. 6-DoF Spline-State-Space (TriS) Model

We extend the basic spline-state-space modeling introduced in [30] from Euclidean-only motion to the complete 6-DoF motion representation. Concretely, the state vector follows  $\underline{x}_k = [(\underline{x}_k^s)^\top, (\underline{x}_k^r)^\top]^\top \in \mathbb{R}^{24}$ , with

$$\begin{aligned} \underline{x}_k^s &= [\underline{s}_{n-3}^\top, \underline{s}_{n-2}^\top, \underline{s}_{n-1}^\top, \underline{s}_n^\top]^\top \in \mathbb{R}^{12} \quad \text{and} \\ \underline{x}_k^r &= [\delta_{n-3}^\top, \delta_{n-2}^\top, \delta_{n-1}^\top, \delta_n^\top]^\top \in \mathbb{R}^{12} \end{aligned} \quad (10)$$

comprising the position recurrent control points (RCPs) in (2) and increments of orientation RCPs in (6).  $k$  denotes

the time step in state-space modeling, at which overall  $n$  knots are present to span the whole spline trajectory. The continuous-time 6-DoF motion trajectory  $\underline{x}(t)$  in (1) is then established for  $t \in [t_{n-1}, t_n)$  according to (2) and (5), that is further embedded to the state-space model as follows

$$\begin{aligned} \underline{x}_{k+1} &= \mathbf{A}_k \underline{x}_k + \underline{w}_k \\ \underline{z}_k &= h(\underline{x}_k; t_k) + \underline{v}_k. \end{aligned} \quad (11)$$

The state vector  $\underline{x}_k \in \mathbb{R}^{24}$  is defined in (10). We propose a linear process model for system propagation, where the transition matrix  $\mathbf{A}_k \in \mathbb{R}^{24 \times 24}$  is kept to be constant and can be configured according to the specific use case.  $\underline{z}_k$  denotes the sensor measurement. The nonlinear observation function  $h(\underline{x}_k; t_k)$  maps the discrete-time state to the measurement domain through kinematic interpolation at timestamp  $t_k$  according to Sec. II-C. See Fig. 2 for the conceptual illustration. Furthermore,  $\underline{w}_k$  and  $\underline{v}_k$  denote additive process and measurement zero-mean noise terms with respective covariances  $\mathbf{Q}$  and  $\mathbf{R}$ . Note in (10) we exploit the RCP increments  $\{\delta_i\}_{i=n-3}^n$  to represent orientation states, rather than the RCPs themselves. The rationale here is to mitigate the nonlinearity associated with the quaternion manifold, thereby avoiding error-state formulations and reducing overall nonlinearity in state estimation.

### B. Jacobians w.r.t. the State Vector

Given the 6-DoF TriS model proposed in Sec. III-A, we further provide the Jacobians of the B-spline kinematics  $\dot{\underline{x}}(t)$  w.r.t. the state components in (10) to facilitate recursive estimation. According to (8), the Jacobian of the position kinematics  $\dot{\mathcal{J}}(t)$  is given by  $\partial \dot{\mathcal{J}}(t) / \partial \underline{x}_k^s = \dot{\mathbf{A}}$  for temporal derivatives up to the second order. The Jacobian of orientation spline  $\underline{r}(t)$  w.r.t. orientation state  $\underline{x}_k^r$  in (10) follows

$$\frac{\partial \underline{r}(t)}{\partial \underline{x}_k^r} = \left[ \frac{\partial \underline{r}(t)}{\partial \delta_{n-3}}, \frac{\partial \underline{r}(t)}{\partial \delta_{n-2}}, \frac{\partial \underline{r}(t)}{\partial \delta_{n-1}}, \frac{\partial \underline{r}(t)}{\partial \delta_n} \right] \in \mathbb{R}^{4 \times 12}, \quad (12)$$

with each block matrix being the Jacobian w.r.t. the increment of orientation RCPs given by

$$\frac{\partial \underline{r}(t)}{\partial \delta_i} = \lambda_i \mathbf{Q}_{\leftarrow}^{\leftarrow} \mathbf{Q}_{\rightarrow}^{\rightarrow} \frac{\partial \text{Exp}_{\mathbf{1}}(\underline{v})}{\partial \underline{v}} \Big|_{\underline{v}=\lambda_i \delta_i}, \quad i = n-3, \dots, n.$$

For brevity, we exploit the substitutions

$$\mathbf{Q}_{\leftarrow}^{\leftarrow} = \mathcal{Q}^{\leftarrow}(\underline{r}_{n-4} \otimes \prod_{j=n-3}^{i-1} \underline{e}_j) \quad \text{and} \quad \mathbf{Q}_{\rightarrow}^{\rightarrow} = \mathcal{Q}^{\rightarrow}(\prod_{j=i+1}^n \underline{e}_j),$$

where  $\mathcal{Q}^{\leftarrow}(\cdot)$  and  $\mathcal{Q}^{\rightarrow}(\cdot)$  denote the left and right matrix expressions of quaternion. Derivation of the partial derivative  $\partial \text{Exp}_{\mathbf{1}}(\underline{v}) / \partial \underline{v}$  is provided in [24, Eq. (19)]. Furthermore, the Jacobian of the angular velocity function  $\underline{\omega}(t)$  in (9) follows

$$\frac{\partial \underline{\omega}(t)}{\partial \underline{x}_k^r} = \left[ \frac{\partial \underline{\omega}(t)}{\partial \delta_{n-3}}, \frac{\partial \underline{\omega}(t)}{\partial \delta_{n-2}}, \frac{\partial \underline{\omega}(t)}{\partial \delta_{n-1}}, \frac{\partial \underline{\omega}(t)}{\partial \delta_n} \right] \in \mathbb{R}^{3 \times 12}, \quad (13)$$

**Algorithm 1:** Recursive Spline Estimator (RESPLE)

---

**Input:** previous posterior  $\hat{\mathbf{x}}_{k-1|k-1}$ ,  $\mathbf{P}_{k-1|k-1}$ ,  
measurement  $\mathbf{z}_k$  at timestamp  $t_k^z$ , maximum  
iteration  $n_{\max}$ , convergence threshold  $\epsilon$

**Output:** posterior estimate  $\hat{\mathbf{x}}_{k|k}$ ,  $\mathbf{P}_{k|k}$

```

/* Prediction */
1 if  $t_k^z < t_n$  then
2    $\mathbf{A}_{k-1} \leftarrow \mathbf{I}_{24}$ ; // random walk
3 else
4    $\mathbf{A}_{k-1} \leftarrow \mathbf{A}$ ; // knot extension
5  $\hat{\mathbf{x}}_{k|k-1} \leftarrow \mathbf{A}_{k-1} \hat{\mathbf{x}}_{k-1|k-1}$ ;
6  $\mathbf{P}_{k|k-1} \leftarrow \mathbf{A}_{k-1} \mathbf{P}_{k-1|k-1} \mathbf{A}_{k-1}^\top + \mathbf{Q}_{k-1}$ ;
/* Iterated Update */
7  $j \leftarrow 0$ ,  $\hat{\mathbf{x}}_j \leftarrow \hat{\mathbf{x}}_{k|k-1}$ ;
8 while true do
9    $\gamma_j \leftarrow \mathbf{z}_k - h(\hat{\mathbf{x}}_j; t_k^z)$ ;
10   $\mathbf{H}_j \leftarrow \text{computeJacobian}(\hat{\mathbf{x}}_j, t_k^z)$ ;
11  if  $\dim(\mathbf{z}_k) \leq \dim(\hat{\mathbf{x}}_{k|k-1})$  then
12     $\mathbf{K}_j \leftarrow \mathbf{P}_{k|k-1} \mathbf{H}_j^\top (\mathbf{H}_j \mathbf{P}_{k|k-1} \mathbf{H}_j^\top + \mathbf{R}_k)^{-1}$ ;
13  else
14     $\mathbf{K}_j \leftarrow (\mathbf{H}_j^\top \mathbf{R}_k^{-1} \mathbf{H}_j + \mathbf{P}_{k|k-1}^{-1})^{-1} \mathbf{H}_j^\top \mathbf{R}_k^{-1}$ ;
15   $\delta \mathbf{x}_j \leftarrow \mathbf{K}_j \gamma_j - (\mathbf{I} - \mathbf{K}_j \mathbf{H}_j) (\hat{\mathbf{x}}_j - \hat{\mathbf{x}}_{k|k-1})$ ;
16   $\hat{\mathbf{x}}_{j+1} \leftarrow \hat{\mathbf{x}}_j + \delta \mathbf{x}_j$ ;
17  if  $\|\delta \mathbf{x}_j\| < \epsilon$  or  $j + 1 = n_{\max}$  then
18    break;
19   $j \leftarrow j + 1$ ;
20  $\hat{\mathbf{x}}_{k|k} \leftarrow \hat{\mathbf{x}}_{j+1}$ ;
21  $\mathbf{P}_{k|k} \leftarrow (\mathbf{I} - \mathbf{K}_j \mathbf{H}_j) \mathbf{P}_{k|k-1}$ ;
22 return  $\hat{\mathbf{x}}_{k|k}$ ,  $\mathbf{P}_{k|k}$ 

```

---

where the terms are derived as

$$\begin{aligned} \frac{\partial \omega(t)}{\partial \underline{\delta}_{n-2}} &= \frac{\partial \omega(t)}{\partial \omega_1(t)} \frac{\partial \omega_1(t)}{\partial \underline{\delta}_{n-2}} = 2\lambda_{n-2} \mathcal{R}(\underline{e}_n^{-1}) \mathcal{R}(\underline{e}_{n-1}^{-1}), \\ \frac{\partial \omega(t)}{\partial \underline{\delta}_{n-3}} &= \mathbf{0}_3, \quad \frac{\partial \omega(t)}{\partial \underline{\delta}_n} = \mathcal{F}_n(\omega_2(t)), \\ \frac{\partial \omega(t)}{\partial \underline{\delta}_{n-1}} &= \frac{\partial \omega(t)}{\partial \omega_2(t)} \frac{\partial \omega_2(t)}{\partial \underline{\delta}_{n-1}} = \mathcal{R}(\underline{e}_n^{-1}) \mathcal{F}_{n-1}(\omega_1(t)), \quad \text{with} \\ \mathcal{F}_i(\underline{v}) &= \lambda_i \frac{\partial(\underline{e}_i^{-1} \bullet \underline{v} \bullet \underline{e}_i)}{\partial \underline{e}_i} \frac{\partial \underline{e}_i}{\partial (\lambda_i \underline{\delta}_i)} + 2\lambda_i \mathbf{I}_3, \quad i = n-1, n. \end{aligned}$$

The function  $\mathcal{R}(\cdot)$  maps a quaternion to its corresponding rotation matrix. The partial derivative  $\partial(\underline{e}_i^{-1} \bullet \underline{v} \bullet \underline{e}_i) / \partial \underline{e}_i$  can be computed according to [7, Eq. (174)].

### C. Recursive Bayesian Estimation on 6-DoF B-Spline

Based on the 6-DoF TriS model proposed in (11), we now establish the recursive spline estimator by modifying the iterated EKF, as outlined in Alg. 1 and elaborated below.

1) *Prediction:* Upon receiving a new measurement  $\mathbf{z}_k$ , we compute the predicted prior mean and covariance as

$$\begin{aligned} \hat{\mathbf{x}}_{k|k-1} &= \mathbf{A}_{k-1} \hat{\mathbf{x}}_{k-1|k-1}, \\ \mathbf{P}_{k|k-1} &= \mathbf{A}_{k-1} \mathbf{P}_{k-1|k-1} \mathbf{A}_{k-1}^\top + \mathbf{Q}_{k-1}, \end{aligned} \quad (14)$$

with  $\hat{\mathbf{x}}_{k-1|k-1}$  and covariance  $\mathbf{P}_{k-1|k-1}$  being the previous posterior mean and covariance, respectively. The transition matrix  $\mathbf{A}_{k-1}$  is selected according to the measurement timestamp. If  $\mathbf{z}_k$  falls within the current spline time span  $t_n$ , the knots remain the same number by setting  $\mathbf{A}_{k-1} = \mathbf{I}_{24}$  as a random walk. Otherwise, we add a new control point to extend the current time span to  $t_n + \tau$  by using a non-identity transition matrix  $\mathbf{A}_{k-1} = \mathbf{A}$ , which will be specified in Sec. IV-B for LiDAR-based odometry.

2) *Iterated Update:* The iterations within the update step are initialized using the predicted prior, i.e.,  $\hat{\mathbf{x}}_j = \hat{\mathbf{x}}_{k|k-1}$  for  $j = 0$ . At each iteration, we compute the observation function's Jacobian  $\mathbf{H}_j$  at  $t_k^z$  w.r.t. current RCPs via the chain rule composing sensor-specific model and the Jacobians of spline kinematics given in Sec. III-B. The current state estimate can be updated according to  $\hat{\mathbf{x}}_{j+1} = \hat{\mathbf{x}}_j + \delta \mathbf{x}_j$ , with the increment  $\delta \mathbf{x}_j$  given by

$$\begin{aligned} \delta \mathbf{x}_j &= \mathbf{K}_j (\mathbf{z}_k - h(\hat{\mathbf{x}}_j)) - (\mathbf{I} - \mathbf{K}_j \mathbf{H}_j) (\hat{\mathbf{x}}_j - \hat{\mathbf{x}}_{k|k-1}), \\ \text{with } \mathbf{K}_j &= \mathbf{P}_{k|k-1} \mathbf{H}_j^\top (\mathbf{H}_j \mathbf{P}_{k|k-1} \mathbf{H}_j^\top + \mathbf{R}_k)^{-1} \end{aligned}$$

denoting the standard Kalman gain at the  $j$ -th iteration, and  $\mathbf{R}_k$  the covariance matrix of measurement noise. In the case of high-dimensional measurement  $\mathbf{z}_k$  (higher than the state vector), the Kalman gain from [5] is adopted, namely,

$$\mathbf{K}_j = (\mathbf{H}_j^\top \mathbf{R}_k^{-1} \mathbf{H}_j + \mathbf{P}_{k|k-1}^{-1})^{-1} \mathbf{H}_j^\top \mathbf{R}_k^{-1}.$$

This avoids the inversion of the high-dimensional matrix associated with the measurement space, while leveraging the block-diagonal structure of  $\mathbf{R}_k^{-1}$  for efficient computation. The iteration terminates when the increment  $\|\delta \mathbf{x}_j\|$  is sufficiently small or the maximum iteration is reached, yielding the posterior mean and covariance  $\hat{\mathbf{x}}_{k|k} = \hat{\mathbf{x}}_{j+1}$  and  $\mathbf{P}_{k|k} = (\mathbf{I} - \mathbf{K}_j \mathbf{H}_j) \mathbf{P}_{k|k-1}$ , respectively.

## IV. LIDAR-BASED ODOMETRY USING RESPLE

We now customize the proposed RESPLE framework to egomotion estimation in a generic multi-LiDAR-inertial setting. The following state vector is set up accordingly

$$\mathbf{x}_k = [(\underline{x}_k^s)^\top, (\underline{x}_k^r)^\top, \underline{b}_{\text{acc}}^\top, \underline{b}_{\text{gyro}}^\top]^\top \in \mathbb{R}^{30}, \quad (15)$$

where  $\underline{x}_k^s$  and  $\underline{x}_k^r$  are the RCP components defined in (10) for representing the IMU body spline trajectory w.r.t. world frame.  $\underline{b}_{\text{acc}}$  and  $\underline{b}_{\text{gyro}}$  denote accelerometer and gyroscope biases within the time span of RCPs, respectively.

### A. System Pipeline

The proposed RESPLE-based multi-LiDAR-inertial odometry system is illustrated in Fig. 3. Given the multi-LiDAR input, point clouds are first downsampled using voxel grids and, together with IMU readings, queued into an observation batch  $\{\mathbf{z}_i^o\}_{i=1}^m$  according to their exact timestamps  $\{t_i^o\}_{i=1}^m$ .

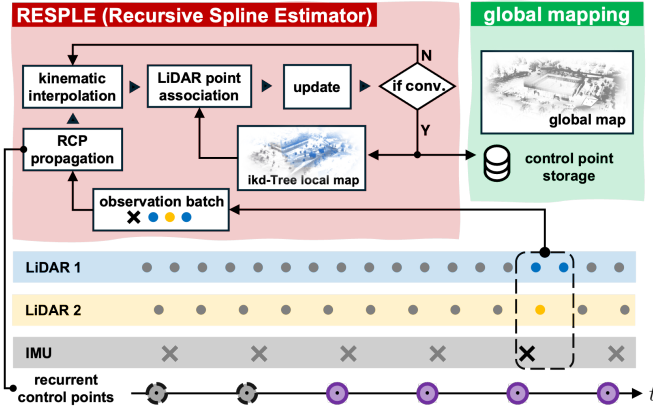


Fig. 3: RESPLE-based multi-LiDAR-inertial odometry.

The superscript  $\circ$  here is an umbrella term for LiDAR (L) and IMU (I) observations. The observation batch size is bounded by a predefined threshold and the time span of the latest knot. Depending on the latest measurement's timestamp, we perform prediction on RCPs through either extension or random walk (Sec. III-C). We further perform kinematic interpolations at the exact timestamps of multi-sensor data points. Each LiDAR point is retrieved within the world frame without explicit de-skewing, followed by association to a spatial local map managed by the ikd-Tree [5]. Once the measurement model in (11) is established, we perform iterated update to obtain posterior estimates of the RCPs. As time progresses, active RCPs transition into idle state, and corresponding LiDAR points are interpolated for maintaining the local map as well as the global trajectory and map.

### B. RESPLE Prediction

We now concretize the non-identity transition matrix  $\mathbf{A}$  for (14) in the case of knot extension. Various principles can be applied to predict the RCP coordinates at the newly added knot; here, we adopt a straightforward strategy that preserves the translational and angular velocities of a preceding RCP. This yields the block-diagonal transition matrix  $\mathbf{A} = \text{diag}(\mathbf{A}_s, \mathbf{A}_r, \mathbf{I}_3, \mathbf{I}_3)$ , with the translational and rotational submatrices as follows

$$\mathbf{A}_s = \begin{bmatrix} \mathbf{0}_3 & \mathbf{I}_3 & \mathbf{0}_3 & \mathbf{0}_3 \\ \mathbf{0}_3 & \mathbf{0}_3 & \mathbf{I}_3 & \mathbf{0}_3 \\ \mathbf{0}_3 & \mathbf{0}_3 & \mathbf{0}_3 & \mathbf{I}_3 \\ -\mathbf{I}_3 & \mathbf{0}_3 & 2\mathbf{I}_3 & \mathbf{0}_3 \end{bmatrix} \quad \text{and} \quad \mathbf{A}_r = \begin{bmatrix} \mathbf{0}_3 & \mathbf{I}_3 & \mathbf{0}_3 & \mathbf{0}_3 \\ \mathbf{0}_3 & \mathbf{0}_3 & \mathbf{I}_3 & \mathbf{0}_3 \\ \mathbf{0}_3 & \mathbf{0}_3 & \mathbf{0}_3 & \mathbf{I}_3 \\ \mathbf{0}_3 & \mathbf{I}_3 & \mathbf{0}_3 & \mathbf{0}_3 \end{bmatrix}. \quad (16)$$

### C. REPLE Update

The basic design in RESPLE processes sensor measurements in a point-wise manner. To ensure real-world runtime efficiency and robustness, a sequence of multi-sensor measurements are temporally stacked into an observation batch  $\tilde{\mathbf{z}}_k = [(\tilde{\mathbf{z}}_1^\circ)^\top, \dots, (\tilde{\mathbf{z}}_m^\circ)^\top]^\top$  w.r.t. their exact timestamps  $\{t_i\}_{i=1}^m$ . Accordingly, we concatenate their Jacobians temporally for iterated update, i.e.,  $\mathbf{H}_j = [(\mathbf{H}_1^\circ)^\top, \dots, (\mathbf{H}_m^\circ)^\top]^\top$ , with  $j$  denoting the iteration index. The LiDAR and IMU measurement models are concretized as follows.

1) *LiDAR point-to-plane metric*: Given a LiDAR point observed at timestamp  $t_i$  and its coordinates  $p_i^\top$  in the LiDAR frame, we establish an observation function for (11) based

on point-to-plane distance as follows

$$h_i^\top(x_k, t_i) = \underline{n}_i^\top (\mathcal{R}(t_i) p_i^\top + \mathcal{s}(t_i) - \underline{\alpha}_i). \quad (17)$$

$p_i^\top = \mathbf{R}_L^\top p_i^L + \underline{s}_L^\top$  transforms the point from LiDAR to IMU body frame through the extrinsic  $\mathbf{R}_L^\top \in \text{SO}(3)$  and  $\underline{s}_L^\top \in \mathbb{R}^3$ . This point is further transformed to world frame through interpolation on the 6-DoF spline trajectory in (1) at  $t_i$ , where the rotation matrix  $\mathcal{R}(t_i) \in \text{SO}(3)$  is applied given quaternion  $r(t_i)$ . We further associate it to the nearest neighbor  $\underline{\alpha}_i$  in the local map through ikd-Tree [5], where a plane is fitted using  $N$  points (e.g.,  $N = 5$ ) in the vicinity. The point-to-plane distance is then computed with the normal vector  $\underline{n}_i$  of the associated plane. Correspondingly, the Jacobian of (17) w.r.t. the state vector (15) is derived as

$$\mathbf{H}_i^L = \left[ \underline{n}_i^\top \mathbf{A}, \underline{n}_i^\top \frac{\partial \mathcal{R}(t_i) p_i^\top}{\partial r(t_i)} \frac{\partial r(t_i)}{\partial \underline{x}_k}, \mathbf{0}_3^\top, \mathbf{0}_3^\top \right] \in \mathbb{R}^{1 \times 30},$$

where  $\partial r(t_i) / \partial \underline{x}_k$  is provided in (12). For outlier rejection, we require the metric's variance estimate  $\mathbf{H}_i^L \mathbf{P}_{k|k-1} (\mathbf{H}_i^L)^\top + \mathbf{R}^L$  to be below a predefined threshold. Here,  $\mathbf{R}^L$  denotes the LiDAR noise variance, and  $\mathbf{P}_{k|k-1}$  is the prior covariance obtained directly from the RESPLE prediction.

2) *IMU metric*: Suppose an IMU measurement  $\tilde{\mathbf{z}}_i^\top = [(\tilde{\mathbf{z}}_i^{\text{acc}})^\top, (\tilde{\mathbf{z}}_i^{\text{gyro}})^\top]^\top$  is received at timestamp  $t_i$  in batch  $\tilde{\mathbf{z}}_k$ , comprising both accelerometer and gyroscope readings. The observation model in (11) is then specified as

$$h_i^\top(\underline{x}_i, t_i) = \begin{bmatrix} \mathcal{R}(t_i)^\top \ddot{\mathbf{a}}(t_i) + \underline{g} + \underline{b}_{\text{acc}} \\ \underline{\omega}(t_i) + \underline{b}_{\text{gyro}} \end{bmatrix}, \quad (18)$$

where  $\ddot{\mathbf{a}}(t_i)$  and  $\underline{\omega}(t_i)$  denote the acceleration and angular velocity at  $t_i^z$ , expressed in the world and body frames, respectively, according to kinematic interpolations (8) and (9). The acceleration  $\ddot{\mathbf{a}}(t_i)$  is then combined with the gravity vector  $\underline{g}$  and transformed to the IMU body by  $\mathcal{R}(t_i) \in \text{SO}(3)$  obtained via (5). Furthermore, we provide the Jacobian of (18) w.r.t. the state vector (15) as follows

$$\mathbf{H}_i^I = \begin{bmatrix} \mathcal{R}(t_i)^\top \ddot{\mathbf{A}} & \frac{\partial \mathcal{R}(t_i)^\top \ddot{\mathbf{a}}(t_i)}{\partial r(t_i)} \frac{\partial r(t_i)}{\partial \underline{x}_k} & \mathbf{I}_3 & \mathbf{0}_3 \\ \mathbf{0}_{3 \times 12} & \frac{\partial \underline{\omega}(t_i)}{\partial \underline{x}_k} & \mathbf{0}_3 & \mathbf{I}_3 \end{bmatrix} \in \mathbb{R}^{6 \times 30},$$

where  $\partial \underline{\omega}(t_i) / \partial \underline{x}_k$  is given in (13).

### D. Implementation

The proposed LiDAR-based odometry system is developed in C++ as a ROS2 package, with Eigen as the primary external dependency [33], [34]. As illustrated in Fig. 3, our system comprises two ROS nodes: the recursive spline estimator (RESPLE), including data preprocessing and association, and the global mapping module. Our software package is designed to support a variety of multi-sensor configurations for LiDAR (LO), LiDAR-inertial (LIO), multi-LiDAR (MLO) and multi-LiDAR-inertial (MLIO) odometry, sharing RESPLE as the core component for motion estimation.

## V. EVALUATION

We conduct extensive real-world benchmarking involving public datasets and own experiments. All evaluations are conducted using a laptop (Intel i7-12800H CPU, 64GB RAM) running Ubuntu 22.04.

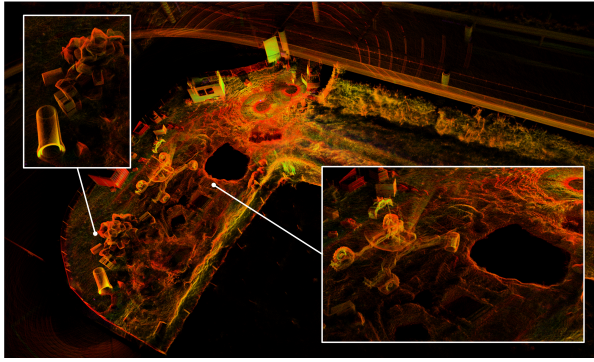


Fig. 4: RESPLE-MLO tested on GrandTour HTH.

### A. Benchmarking Setup

We include public datasets NTU VIRAL [35], MCD [36], and GrandTour [37], and our own experimental dataset *HelmDyn* for evaluations, as described in Tab. I for various mobile platforms, scenarios, and sensor configurations. RESPLE (R) is compared against several state-of-the-art open-source systems: KISS-ICP [6] (K-ICP), Traj-LO (T-LO) [17], CTE-MLO [22] (C-MLO), FAST-LIO2 [5] (F-LIO2), Point-LIO (P-LIO) [13], SLICT2 [25]. Abbreviations in parentheses are used for brevity. In all evaluations, we adopt a knot frequency of 100 Hz and a maximum of 5 iterations for the iterated update. In each dataset, the same parameter set is used without individual tuning, where the observation batch spans 3 to 10 ms. For numerical evaluation of accuracy, the global trajectory estimates are interpolated at timestamps of ground truth. The RMSE of the absolute position error (APE) is then computed using *evo* [38] except for NTU VIRAL, where its official evaluation script is used. We mark failures using  $\times$ , and the best and second-best results with **bold** and underline, respectively.

TABLE I: Datasets for real-world benchmarking.

Dataset	Scenarios	LI Sensors (Adopted)
NTU VIRAL [35]	indoor, outdoor, drone	Ouster OS1-16 (L) VN100 (I)
MCD [36]	large-scale urban, fast, ground vehicle	Livox Mid70 (L) VN100 (I)
GrandTour [37]	wild, urban, underground quadruped robot	Hesai XT32 (L1) Livox Mid360 (L2) built-in L1 (I)
<i>HelmDyn</i> (own experiment)	indoor, dynamic, wearable (helmet)	Livox Mid360 (L) built-in L (I)

### B. Public Datasets

1) *NTU VIRAL*: We adopt the horizontal LiDAR in the dataset and use the official script for evaluation [35]. Shown in Tab. II, our LO system demonstrates superior accuracy over KISS-ICP, CTE-MLO (using 2 LiDARs), and FAST-LIO2 (LIO) on all sequences, and Traj-LO on most (13/18) sequences. Our LO/LIO variants consistently rank among the top two in accuracy (except *spms\_03* with a small margin), without any failures.

TABLE II: APE (RMSE) in meters on NTU VIRAL.

	K-ICP <sup>1</sup>	T-LO <sup>1</sup>	C-MLO <sup>2</sup>	F-LIO2 <sup>3</sup>	R-LO	R-LIO
eee_01	2.220	0.055	0.08	0.069	<u>0.044</u>	<b>0.038</b>
eee_02	1.570	0.039	0.07	0.069	<u>0.023</u>	<b>0.022</b>
eee_03	1.014	<u>0.035</u>	0.12	0.111	0.046	<b>0.033</b>
nya_01	0.628	0.047	0.06	0.053	<u>0.033</u>	<b>0.031</b>
nya_02	1.500	0.052	0.09	0.090	<b>0.036</b>	<b>0.036</b>
nya_03	1.272	0.050	0.10	0.108	<u>0.037</u>	<b>0.032</b>
rtp_01	3.663	<b>0.050</b>	0.13	0.125	<u>0.059</u>	<u>0.059</u>
rtp_02	1.970	<u>0.058</u>	0.14	0.131	0.071	<b>0.048</b>
rtp_03	2.382	<u>0.057</u>	0.14	0.137	<b>0.054</b>	0.113
sbs_01	0.917	0.048	0.09	0.086	<u>0.040</u>	<b>0.034</b>
sbs_02	1.312	<u>0.039</u>	0.08	0.078	0.104	<b>0.035</b>
sbs_03	1.030	0.039	0.09	0.076	<b>0.036</b>	<b>0.036</b>
spms_01	8.493	<u>0.121</u>	0.21	0.210	<b>0.109</b>	0.133
spms_02	$\times$	$\times$	0.33	0.336	<u>0.127</u>	<b>0.107</b>
spms_03	5.451	<b>0.103</b>	<u>0.20</u>	0.217	0.217	0.236
tnp_01	2.305	0.505	0.09	0.090	<b>0.052</b>	<u>0.055</u>
tnp_02	2.405	0.607	0.09	0.110	<u>0.070</u>	<b>0.065</b>
tnp_03	0.799	0.101	0.10	0.089	<u>0.050</u>	<b>0.047</b>

<sup>1,2,3</sup>Results taken from [17], [22] and [25].

2) *MCD*: We select 6 fast, large-scale sequences, covering both day and night scenarios [36] listed in Tab. III. Compared to Traj-LO, CTE-MLO, and FAST-LIO2, the RESPLE-based LO/LIO systems are among the top two in accuracy across all sequences, without experiencing any failures.

TABLE III: APE (RMSE) in meters on MCD.

	T-LO	C-MLO	F-LIO2 <sup>1</sup>	R-LO	R-LIO
ntu_day_01	$\times$	72.200	<u>0.901</u>	0.910	<b>0.412</b>
ntu_day_02	0.194	4.640	0.185	<b>0.176</b>	<u>0.178</u>
ntu_day_10	<b>1.129</b>	24.173	1.975	<u>1.377</u>	1.838
ntu_night_04	<u>0.427</u>	28.519	0.902	0.693	<b>0.345</b>
ntu_night_08	<u>0.950</u>	64.387	1.002	0.953	<b>0.880</b>
ntu_night_13	$\times$	17.791	1.288	<b>0.520</b>	<u>0.533</u>

<sup>1</sup>Results taken from [25].

3) *GrandTour*: The GrandTour [37] is a new legged robotics dataset of immense scale and diversity. An ANYmal D quadruped robot equipped with a new open-source multi-sensor rig *Boxi* [39] traversed 71 Swiss environments under diverse conditions, in which the robot walked a total of 15 km over 8 hours. We select 2 sequences recorded underground (JTL/S), 1 urban sequence (HTH) and 5 in the wild (forests and mountains). The ground truth used for these sequences was obtained by tracking the position of a reflector prism with a Leica Geosystems MS60 Total Station. The sequences present challenges due to dynamic motions and cluttered or geometrically degenerate scenes. Traj-LO, CTE-MLO and FAST-LIO2 exhibit multiple failures. Our LiDAR-only variant performs well with only one failure. Moreover, adding an additional LiDAR and IMU within RESPLE can significantly improve estimation accuracy and robustness. Exemplary runs of RESPLE-MLO on LFH2 and HTH are illustrated in Fig. 1-(B) and Fig. 4, respectively.

### C. Own Experiments

*HelmDyn*: We conduct own experiments using a Livox Mid360 mounted on a helmet, as shown in Fig. 5-(A),

**TABLE IV:** APE (RMSE) in meters on GrandTour.

	T-LO	C-MLO	F-LIO2	R-LO	R-MLO	R-LIO	R-MLIO
	L1	L1+L2	L1+I	L1	L1+L2	L1+I	L1+L2+I
JTL	0.046	0.197	<b>X</b>	0.035	<b>0.026</b>	0.030	<u>0.029</u>
JTS	<b>0.074</b>	0.411	2.585	0.256	<u>0.088</u>	0.131	0.093
GR	<b>X</b>	<b>X</b>	5.522	<u>0.042</u>	0.054	<b>0.038</b>	0.046
PKH2	<b>X</b>	<b>X</b>	<b>X</b>	<b>X</b>	0.059	<u>0.051</u>	<b>0.047</b>
HTH	0.045	0.040	0.151	<u>0.026</u>	0.027	<b>0.024</b>	0.030
TB	0.047	<b>X</b>	0.218	0.040	<u>0.031</u>	0.036	<b>0.026</b>
LFH2	0.044	<b>X</b>	0.442	<u>0.018</u>	0.029	<b>0.015</b>	0.032
AFH2	0.043	<b>X</b>	3.086	0.044	<u>0.039</u>	0.047	<b>0.035</b>

**Abbr.:** JTL/S (Jungfrauoch Tunnel Large/Small), GR (Grindelwald Riverside), PKH (Pilatus Kulm Hike), HTH (HEAP Testsite Hoenggerberg), TB (Triemli Biketrail), L/AFH (Leimbach/Albisguetli Forest Hike).



**Fig. 5:** Mobile platforms in own experiments.

operated in a  $12 \times 12 \times 8 \text{ m}^3$  cubic space along with dynamic movements combining walking, running, jumping, and in-hand waving. Ground truth trajectories are acquired using a high-precision (submillimeter), low-latency motion capture system consisting of 12 Oqus 700+ and 8 Arqus A12 Qualisys cameras with passive markers. Across the entire HelmDyn (Helmet Dynamic) dataset, RESPLE consistently outperforms state-of-the-art methods despite dynamic motions. We compare with Point-LIO considering its capability of handling aggressive motions. SLICT2 employs surfel-based global map for odometry, thus we include it here for comparison in small-scale scenarios (rather than MCD). A few exemplary runs of RESPLE-LO are illustrated in Fig. 6.

**TABLE V:** APE (RMSE) in meters on HelmDyn.

	T-LO	C-MLO	F-LIO2	P-LIO	SLICT2	R-LO	R-LIO
HD_01	0.081	0.050	0.062	0.109	0.086	<u>0.041</u>	<b>0.040</b>
HD_02	3.667	<b>X</b>	0.073	5.206	0.046	<b>0.033</b>	<u>0.034</u>
HD_03	0.043	0.031	0.033	0.048	0.046	<u>0.021</u>	<b>0.020</b>
HD_04	0.089	<u>0.035</u>	0.054	0.100	0.037	<b>0.034</b>	<b>0.034</b>
HD_05	0.052	0.027	0.028	0.055	0.057	<u>0.021</u>	<b>0.020</b>
HD_06	0.059	0.030	0.039	0.063	0.057	<b>0.021</b>	<b>0.021</b>
HD_07	3.671	0.040	0.052	0.066	0.056	<b>0.031</b>	<b>0.031</b>
HD_08	0.054	0.029	0.030	0.061	0.048	<b>0.019</b>	<u>0.020</u>
HD_09	0.063	0.036	0.042	0.063	0.063	<b>0.025</b>	<u>0.026</u>
HD_10	1.616	<b>X</b>	0.063	4.253	0.054	<u>0.034</u>	<b>0.033</b>

*R-Campus:* We further evaluate our systems using a Livox Avia mounted on a bipedal wheeled robot [40], as illustrated in Fig. 5-(B). It operates within a campus environment over a trajectory of approximately 1400 m at 1.2 m/s. The route starts and ends at the same location. Our RESPLE-based LO and LIO achieve end-to-end errors of 0.28 m and

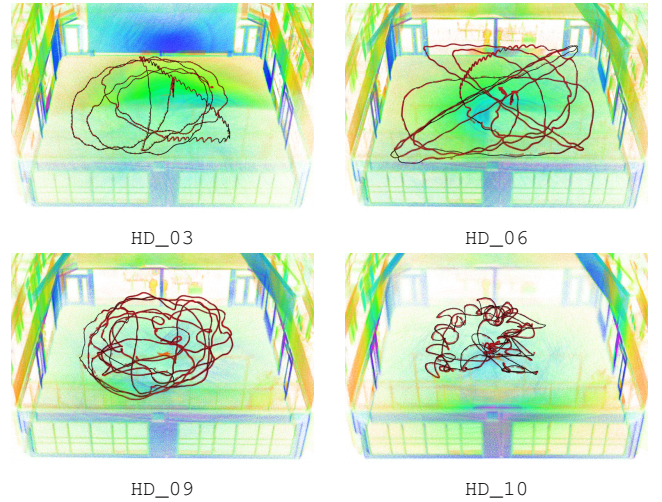


**Fig. 6:** RESPLE-LO tested on HelmDyn. Black and red curves are estimate and ground truth, respectively.

0.27 m, respectively – significantly better than FAST-LIO2 (2.70 m) and Traj-LO (80.31 m).

#### D. Runtime Analysis

For analyzing the runtime efficiency of RESPLE, we configure the observation batch with a time span strictly equal to the knot interval (10 ms). Three sequences are selected from the earlier benchmarking as listed in Tab. VI. We present the average number of LiDAR points and processing time of the RESPLE node in Fig. 3, including the iterated update, in each step. Across all (multi-)sensor settings, our proposed systems remain real-time capable, with an estimated theoretical speed ranging from 1.5 to 7.5 times of real time.

**TABLE VI:** Runtime for RESPLE-based LiDAR odometry.

Sequence	#Pts	Settings	Processing Time (ms)	
			Iterated Update	Total
HD_03	295	LO/LIO	1.88/2.16	2.25/2.55
eee_01	205	LO/LIO	0.94/1.28	1.28/1.76
LF Hike 2	621	MLO/MLIO	4.88/4.43	6.79/6.47

#### E. Discussion

Without LiDAR degeneracy, RESPLE performs comparably in both LO and LIO settings in terms of accuracy, even with dynamic motions, as demonstrated in NTU VIRAL, MCD, and HelmDyn, where RESPLE-LO usually consumes less time than the LIO variant. Under LiDAR degeneracy, adding additional IMU and LiDAR sensors can improve estimation accuracy and robustness as demonstrated in GrandTour. The filtering-based design and ikd-Tree-based local map management may also affect the odometry performance in large-scale scenarios, especially under conditions with LiDAR degeneracy.

## VI. CONCLUSION

In this paper, we presented RESPLE, the first recursive B-spline estimation framework for continuous-time 6-DoF dynamic motion estimation. The state vector comprises the position RCPs and orientation RCP increments, enabling 6-DoF B-spline estimation through a modified iterated EKF without error-state formulations. Using RESPLE, we further develop a versatile, unified suite of direct LiDAR-based odometry systems for various multi-sensor settings (LO, LIO, MLO, and MLIO). Our systems outperform state-of-the-art solutions in terms of accuracy and robustness in diverse real-world application scenarios, while attaining real-time efficiency. For future work, we plan to integrate visual sensors into the RESPLE-based sensor fusion pipeline to better handle the degeneracy cases and to incorporate a backend for global correction. Additionally, it is promising to explore downstream tasks of estimation, such as motion planning, that can benefit from RESPLE's uncertainty-aware, continuous-time trajectory estimates.

## REFERENCES

- [1] A. Geiger, P. Lenz, C. Stiller, and R. Urtasun, "Vision Meets Robotics: The KITTI Dataset," *The International Journal of Robotics Research*, vol. 32, no. 11, pp. 1231–1237, 2013.
- [2] M. Tranzatto, T. Miki, M. Dharmadhikari, L. Bernreiter, M. Kulkarni, F. Mascariich, O. Andersson, S. Khattak, M. Hutter, R. Siegwart, et al., "CERBERUS in the DARPA subterranean challenge," *Science Robotics*, vol. 7, no. 66, p. eabp9742, 2022.
- [3] T. Miki, J. Lee, J. Hwangbo, L. Wellhausen, V. Koltun, and M. Hutter, "Learning robust perceptive locomotion for quadrupedal robots in the wild," *Science Robotics*, vol. 7, no. 62, p. eabk2822, 2022.
- [4] K. Li, M. Li, and U. D. Hanebeck, "Towards High-Performance Solid-State-LiDAR-Inertial Odometry and Mapping," *IEEE Robotics and Automation Letters*, vol. 6, no. 3, pp. 5167–5174, 2021.
- [5] W. Xu, Y. Cai, D. He, J. Lin, and F. Zhang, "FAST-LIO2: Fast direct LiDAR-inertial odometry," *IEEE Transactions on Robotics*, vol. 38, no. 4, pp. 2053–2073, 2022.
- [6] I. Vizzo, T. Guadagnino, B. Mersch, L. Wiesmann, J. Behley, and C. Stachniss, "KISS-ICP: In defense of point-to-point ICP—simple, accurate, and robust registration if done the right way," *IEEE Robotics and Automation Letters*, vol. 8, no. 2, pp. 1029–1036, 2023.
- [7] J. Sola, "Quaternion Kinematics for the Error-State Kalman Filter," *arXiv preprint arXiv:1711.02508*, 2017.
- [8] M. Bloesch, M. Burri, S. Omari, M. Hutter, and R. Siegwart, "Iterated extended Kalman filter based visual-inertial odometry using direct photometric feedback," *The International Journal of Robotics Research*, vol. 36, no. 10, pp. 1053–1072, 2017.
- [9] S. Leutenegger, S. Lynen, M. Bosse, R. Siegwart, and P. Furgale, "Keyframe-based visual-inertial odometry using nonlinear optimization," *The International Journal of Robotics Research*, vol. 34, no. 3, pp. 314–334, 2015.
- [10] T. Qin, P. Li, and S. Shen, "VINS-Mono: A Robust and Versatile Monocular Visual-Inertial State Estimator," *IEEE Transactions on Robotics*, vol. 34, no. 4, pp. 1004–1020, 2018.
- [11] Y. Cai, W. Xu, and F. Zhang, "ikd-Tree: An incremental kd tree for robotic applications," *arXiv preprint arXiv:2102.10808*, 2021.
- [12] C. Bai, T. Xiao, Y. Chen, H. Wang, F. Zhang, and X. Gao, "Fasterlio: Lightweight tightly coupled lidar-inertial odometry using parallel sparse incremental voxels," *IEEE Robotics and Automation Letters*, vol. 7, no. 2, pp. 4861–4868, 2022.
- [13] D. He, W. Xu, N. Chen, F. Kong, C. Yuan, and F. Zhang, "Point-lío: Robust high-bandwidth light detection and ranging inertial odometry," *Advanced Intelligent Systems*, vol. 5, no. 7, p. 2200459, 2023.
- [14] W. Talbot, J. Nubert, T. Tuna, C. Cadena, F. Dümbs, J. Tordesillas, T. D. Barfoot, and M. Hutter, "Continuous-time state estimation methods in robotics: A survey," *arXiv preprint arXiv:2411.03951*, 2024.
- [15] J. Johnson, J. Mangelson, T. Barfoot, and R. Beard, "Continuous-time trajectory estimation: A comparative study between gaussian process and spline-based approaches," *arXiv preprint arXiv:2402.00399*, 2024.
- [16] J. Zhang and S. Singh, "LOAM: LiDAR odometry and mapping in real-time," *Robotics: Science and Systems X*, 2014.
- [17] X. Zheng and J. Zhu, "Traj-LO: In defense of LiDAR-only odometry using an effective continuous-time trajectory," *IEEE Robotics and Automation Letters*, vol. 9, no. 2, pp. 1961–1968, 2024.
- [18] T. D. Barfoot, *State estimation for robotics*. Cambridge University Press, 2024.
- [19] T.-M. Nguyen, Z. Cao, K. Li, S. Yuan, and L. Xie, "GPTR: Gaussian process trajectory representation for continuous-time motion estimation," *arXiv preprint arXiv:2410.22931*, 2024.
- [20] K. Burnett, Y. Wu, D. J. Yoon, A. P. Schoellig, and T. D. Barfoot, "Are we ready for radar to replace lidar in all-weather mapping and localization?" *IEEE Robotics and Automation Letters*, vol. 7, no. 4, pp. 10328–10335, 2022.
- [21] K. Burnett, A. P. Schoellig, and T. D. Barfoot, "Continuous-Time Radar-Inertial and Lidar-Inertial Odometry Using a Gaussian Process Motion Prior," *IEEE Transactions on Robotics*, vol. 41, pp. 1059–1076, 2025.
- [22] H. Shen, Z. Wu, Y. Hui, W. Wang, Q. Lyu, T. Deng, Y. Zhu, B. Tian, and D. Wang, "CTE-MLO: Continuous-time and efficient multi-LiDAR odometry with localizability-aware point cloud sampling," *IEEE Transactions on Field Robotics*, vol. 2, pp. 165–187, 2025.
- [23] K. Sommer, V. Usenko, D. Schubert, N. Demmel, and D. Cremers, "Efficient Derivative Computation for Cumulative B-Splines on Lie Groups," in *Proceedings of the IEEE/CVF Conference on Computer Vision and Pattern Recognition (CVPR)*, Seattle, WA, USA, June 2020.
- [24] K. Li, Z. Cao, and U. D. Hanebeck, "Continuous-time ultra-wideband-inertial fusion," *IEEE Robotics and Automation Letters*, vol. 8, no. 7, pp. 4338–4345, 2023.
- [25] T.-M. Nguyen, X. Xu, T. Jin, Y. Yang, J. Li, S. Yuan, and L. Xie, "Eigen is all you need: Efficient lidar-inertial continuous-time odometry with internal association," *IEEE Robotics and Automation Letters*, vol. 9, no. 6, pp. 5330–5337, 2024.
- [26] J. Lv, K. Hu, J. Xu, Y. Liu, X. Ma, and X. Zuo, "CLINS: Continuous-Time Trajectory Estimation for LiDAR-Inertial System," in *IEEE/RSJ International Conference on Intelligent Robots and Systems (IROS)*, 2021, pp. 6657–6663.
- [27] J. Lv, X. Lang, J. Xu, M. Wang, Y. Liu, and X. Zuo, "Continuous-time fixed-lag smoothing for lidar-inertial-camera slam," *IEEE/ASME Transactions on Mechatronics*, 2023.
- [28] Y. Lv, Y. Zhang, X. Zhao, W. Li, J. Ning, and Y. Jin, "CTA-LO: Accurate and robust lidar odometry using continuous-time adaptive estimation," in *IEEE International Conference on Robotics and Automation (ICRA)*, 2024, pp. 12034–12040.
- [29] M. Jung, S. Jung, and A. Kim, "Asynchronous multiple lidar-inertial odometry using point-wise inter-lidar uncertainty propagation," *IEEE Robotics and Automation Letters*, vol. 8, no. 7, pp. 4211–4218, 2023.
- [30] K. Li, "On embedding B-splines in recursive state estimation," *arXiv preprint arXiv:2307.00637*, 2023.
- [31] H. Ovrén and P.-E. Forssén, "Trajectory representation and landmark projection for continuous-time structure from motion," *The International Journal of Robotics Research*, vol. 38, no. 6, pp. 686–701, 2019.
- [32] D. Hug, P. Bänninger, I. Alzugaray, and M. Chli, "Continuous-Time Stereo-Inertial Odometry," *IEEE Robotics and Automation Letters*, vol. 7, no. 3, pp. 6455–6462, 2022.
- [33] S. Macenski, T. Foote, B. Gerkey, C. Lalancette, and W. Woodall, "Robot Operating System 2: Design, architecture, and uses in the wild," *Science Robotics*, vol. 7, no. 66, p. eabm6074, 2022.
- [34] G. Guennebaud, B. Jacob, et al., "Eigen v3," <http://eigen.tuxfamily.org>, 2010.
- [35] T.-M. Nguyen, S. Yuan, M. Cao, Y. Lyu, T. H. Nguyen, and L. Xie, "NTU VIRAL: A Visual-Inertial-Ranging-Lidar dataset, from an Aerial Vehicle Viewpoint," *The International Journal of Robotics Research*, vol. 41, no. 3, pp. 270–280, 2022.
- [36] T.-M. Nguyen, S. Yuan, T. H. Nguyen, P. Yin, H. Cao, L. Xie, M. Wozniak, P. Jensfelt, M. Thiel, J. Ziegenbein, and N. Blunder, "MCD: Diverse Large-Scale Multi-Campus Dataset for Robot Perception," in *Proceedings of the IEEE/CVF Conference on Computer Vision and Pattern Recognition*, 2024, pp. 22304–22313.
- [37] J. Frey, T. Tuna, L. F. T. Fu, T. Xu, K. Patterson, M. Fallon, C. Cadena, and M. Hutter, "The GrandTour ETH Zurich Dataset," in *preparation for The International Journal of Robotics Research*, 2025.

- [38] M. Grupp, “evo: Python package for the evaluation of odometry and SLAM.” <https://github.com/MichaelGrupp/evo>, 2017.
- [39] J. Frey, T. Tuna, L. F. T. Fu, C. Weibel, K. Patterson, B. Krummenacher, M. Müller, J. Nubert, M. Fallon, C. Cadena, and M. Hutter, “Boxi: Design decisions in the context of algorithmic performance for robotics,” *Proceedings of Robotics: Science and Systems*, 2025.
- [40] D. Liu, F. Yang, X. Liao, and X. Lyu, “DIABLO: A 6-dof wheeled bipedal robot composed entirely of direct-drive joints,” in *IEEE/RSJ International Conference on Intelligent Robots and Systems (IROS)*, 2024, pp. 3605–3612.